A Chandra-HETG VIEW OF MCG +8-11-11

The Astrophysical Journal, 797:12 (11pp), 2014 December 10 doi:10.1088/0004-637X/797/1/12

A *Chandra*-HETG VIEW OF MCG +8-11-11

K. D. Murphy[1] and M. A. Nowak[2]
[1] Department of Physics, Skidmore College, Saratoga Springs, NY 12866, USA; kmurphy1@skidmore.edu
[2] MIT Kavli Institute for Space Research, 77 Massachusetts Avenue, NE83-653, Cambridge, MA 02139, USA
Received 2014 April 11; accepted 2014 October 6; published 2014 November 19

ABSTRACT

We present a spectral analysis of the 118 ks *Chandra* High Energy Transmission Gratings (HETG) observation of the X-ray bright Seyfert 1.5 galaxy MCG +8-11-11, in conjunction with 100 ks of archival *Suzaku* data, aimed at investigating the signatures of warm absorption and Compton reflection reported from previous *Suzaku* and *XMM-Newton* studies of the source. Contrary to previous results, we find that warm absorption is not required by the data. Instead, we report upper limits on absorption lines that are below previous (marginal) detections. Fe Kα line emission is clearly detected and is likely resolved with $\sigma \sim 0.02$ keV with the HETG data. We applied self-consistent, broadband spectral-fitting models to the *Chandra* and *Suzaku* data to investigate this and other signatures of distant absorption and reflection. Utilizing in particular the `MYTorus` model, we find that the data are consistent with reprocessing by a distant, neutral torus that is marginally Compton-thick ($N_H \sim 10^{24}$cm^{-2}) and out of the line of sight. However, we do not find compelling evidence of a relativistically broadened Fe K emission line, which is often expected from type 1 active galactic nuclei. This is consistent with some, although not all, previous studies of MCG +8-11-11. A well-measured edge is identified by the HETG near 0.5 keV, indicating neutral absorption in the line of sight that is consistent with galactic absorption; however, the absorption may be partially intrinsic to the source. The HETG data are consistent with the presence of a soft excess, a feature that may be missed by considering the *Suzaku* data alone.

Key words: galaxies: active – galaxies: individual (MCG+8-11-11) – galaxies: Seyfert – X-rays: galaxies

Online-only material: color figures

1. INTRODUCTION

The unified model of active galactic nuclei (AGNs) postulates a system of complex components: an inner accretion disk near the black hole responsible for the bulk of the bolometric emission, outer broad and narrow line regions (BLR/NLR), and a putative torus also at outer radii, possibly obscuring the inner emission regions for some viewing angles. Recent X-ray studies have attempted to use the inner accretion flows of these systems to probe the relativistic nature of the black hole (i.e., by measuring relativistically broadened Fe Kα lines; see Reynolds & Nowak 2003 for a review). The interpretation of a broadened line has come under criticism, however, from some authors who point out that the 2–10 keV continuum, and specifically the Fe line and edge region, might be sculpted by the presence of a warm, highly ionized absorber/wind (Miller et al. 2009). Understanding the nature of the highly ionized absorbing wind (whose presence has been recognized since CCD spectroscopic observations with the Advanced Satellite for Cosmology and Astrophysics, ASCA; Reynolds & Fabian 1995) and cold reflection is therefore crucial for both developing global models of AGN systems, as well as for accurately describing relativistic emission from the inner accretion disk.

MCG +8-11-11, a nearby ($z = 0.0205$) Seyfert 1.5 galaxy, is one of the X-ray brightest Seyfert galaxies ever observed ($L_{2-10} \sim 10^{44}$ erg s^{-1}). The broadband X-ray spectrum has historically been described by a power law with a high-energy, exponential cutoff, a strong Fe Kα emission line, a Compton reflection component, and warm absorption (Grandi et al. 1998; Perola et al. 2000); its X-ray spectral shape has not been seen to vary significantly since it was observed by ASCA (Bianchi et al. 2010), although its flux has been observed to vary by a factor of three from its faint to bright end (Soldi et al. 2010). A study of this source with *XMM-Newton* (Matt 2006) was conducted to determine the origin of the Fe K line emission. Evidence of a Compton shoulder associated with the unresolved Fe Kα line emission was found, suggesting, together with the clear reflection component in the continuum, that the emission originated in distant matter that may be Compton-thick. Only a loose upper limit on the ratio of the Compton shoulder, which was modeled ad-hoc with Gaussian line emission, to the Fe Kα line core emission was determined. Marginal detections of Fe Kβ and Ni Kα, likely originating in the same structure, were also reported, but only loose constraints on the ratios of these lines were possible. One of the more puzzling results of this study was the lack of a detection of an underlying broad component (i.e., from the accretion disk) of the Fe Kα emission line, which is expected to be seen in the X-ray spectrum of bright type 1 AGNs, as their inclination angles theoretically afford us an unobscured view of their innermost regions. However, some ambiguity was found: the equivalent width of the Fe Kα line core plus Compton shoulder was found to be ~90 eV, implying either an underabundance of iron or the existence of two reflection regions (i.e., a torus and an ionized accretion disk, the latter providing a reflection hump but not a narrow Fe K emission line; Matt 2006).

The *XMM-Newton* data (Matt 2006) also required (at CCD resolution) the inclusion of a highly ionized warm absorber ($\log \xi \approx 2.7$, $\log N_{\rm H} \approx 23$), as well as an edge in the <1 keV spectrum. A number of possible absorption lines were found in the Reflection Grating Spectrometer (RGS) spectrum, but their identification was ambiguous. However, such a highly ionized absorber would have placed most ionized absorption lines at energies outside of the useful range of the RGS detector. Although the velocity structure could not be deduced from the absorption edges, the velocity structure appeared to be complex.

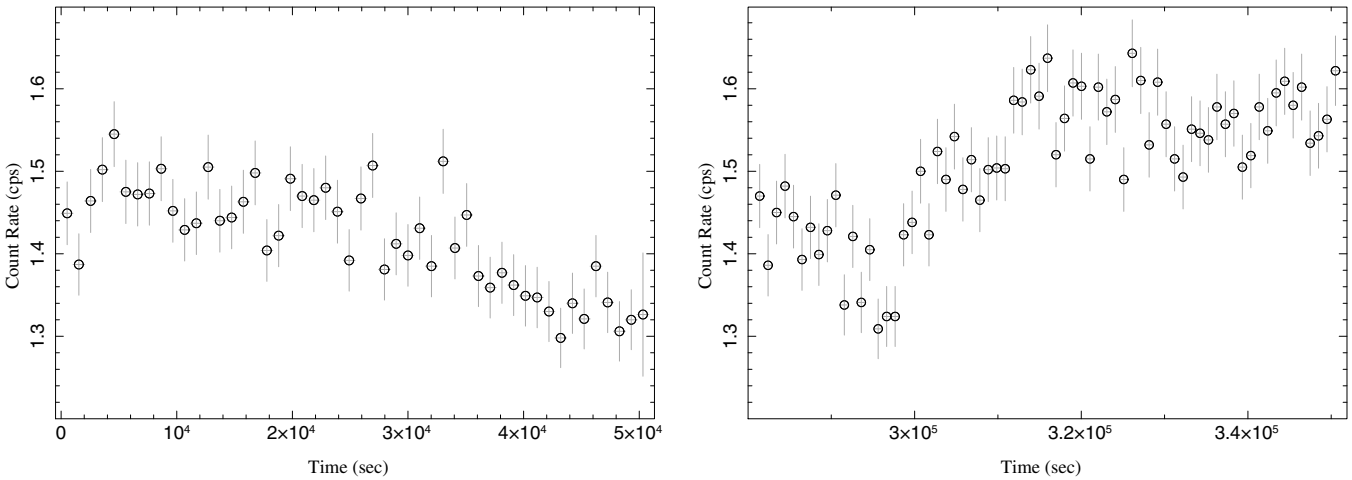

Figure 1. *Chandra*-HETG light curves in 1000 s bins from the combined ±1st orders of the HEG and MEG in the 1.7–25 Å band.

Bianchi et al. (2010) and Patrick et al. (2012) found results consistent with the *XMM-Newton* analysis reported by Matt (2006) in their separate analyses of the same 100 ks *Suzaku* X-ray Imaging Spectrometer (XIS) observation of MCG +8-11-11. Specifically, each found an intrinsic power-law spectrum with a photon index of $\Gamma = 1.7$–1.8, a lack of soft excess, warm absorption in the line of sight (required by spectral curvature at low energies), and significant Compton reflection with a narrow Fe Kα line with equivalent width $\approx$67 eV. Both reported evidence of Fe XXVI line emission; Bianchi et al. (2010) also reported a detection of Fe XXV line emission. However, unlike Matt (2006), Patrick et al. (2012) found that the data require relativistic Fe Kα line emission in addition to narrow line emission. Bianchi et al. (2010) did not find evidence of a relativistically smeared line component when considering XIS data alone; however, such a component became required when the Hard X-ray Detector (HXD) PIN data were included in their analysis. In this case, the reflection fraction became significantly smaller, the (weak) reflection continuum was associated with the accretion disk, and the origin of the narrow Fe K emission was attributed to a Compton-thin region (the BLR).

An analysis of *Swift* with *INTEGRAL* data, together with *Suzaku* data, by Soldi et al. (2010) also pointed to little Compton reflection. (The *Swift* data only placed upper limits of $\lesssim$300 eV on narrow Fe Kα emission.) Both Soldi et al. (2010) and Bianchi et al. (2010) quantified the amount of reflection via the reflection fraction obtained by fitting the PEXRAV model to the broadband data; they found values of $R = 0.2$–0.3 and $R < 0.2$, respectively, in contrast with $R \sim 1$ found by Bianchi et al. (2010) with the XIS data alone. Bianchi et al. (2010) furthermore found that the broadband spectrum indicated subsolar Fe abundance, but noted that there is ambiguity between the iron abundance and the inclination angle of the system. Additional ambiguity was found between the broad Fe Kα line emission and the possible Compton shoulder redward of the narrow Fe Kα line emission.

The common spectral components of the *XMM-Newton*, *Suzaku*, *Swift*, and *INTEGRAL* data, which exhibit 2–10 keV fluxes ranging from 4.6×10^{-11} erg cm^{-2} s^{-1} (*XMM-Newton*; Matt 2006) to 6.4×10^{-11} erg cm^{-2} s^{-1} (*Suzaku*; Bianchi et al. 2010) to as high as 8.1×10^{-11} erg cm^{-2} s^{-1} (*Swift*; Soldi et al. 2010), is the presence of both a power-law continuum whose shape does not strongly vary ($\Gamma \approx 1.7$–1.8) and a narrow Fe Kα line with equivalent width $\approx$70 eV[3]— along with additional complexity at high energies, e.g., from an edge, Fe Kβ emission, and Ni K emission—when there are sufficient statistics to detect such features.

To investigate the presence of absorption lines from a potentially multi-zoned warm absorber as well as to determine the structure and location of the origin of the narrow Fe Kα line emission by disentangling it from the Fe K line complex, we obtained $\approx$118 ks of *Chandra* High Energy Transmission Gratings (HETG) data for MCG +8-11-11. As pointed out by, e.g., Bianchi et al. (2010), the analysis of the X-ray spectrum may yield compromised results if the covered energy band is limited to below 10 keV. We therefore report on our analysis of the *Chandra* data in combination with the archived broadband data from *Suzaku*.

2. OBSERVATIONS AND DATA REDUCTION

2.1. Chandra-HETG

Observations of MCG +8-11-11 were completed on 2010 December 7 (obsid 12861) and 2010 December 10 (ObsID 13200) by the *Chandra* Advanced CCD Imaging Spectrometer (Garmire et al. 2003), using the HETG (Canizares et al. 2005). Exposure times of 49.2 ks and 68.9 ks, respectively, were obtained. Light curves for the two observations are shown in Figure 1, which exhibit little variability over the course of the two observations (substantially less than the factor of three long-term variability).

We used CIAO version 4.4 and CALDB version 4.5.1 to run a standard extraction of the first-order High Energy Gratings (HEG) and Medium Energy Gratings (MEG) data and to create the response files. We first investigated each of the HEG and MEG data sets for the two observations separately. Finding good agreement among the spectra, and in order to achieve the highest signal-to-noise ratio possible, we co-added the data (using the `combine_data sets` function in the `Interactive Spectral Interpretation System`; Houck & Denicola 2000) from the two observations and from the

[3] In terms of absolute line flux, the *Suzaku* detected line is 50% stronger than the line flux quoted by Matt (2006) for the *XMM-Newton* data. However, it is not clear to what extent these differences are systematic as regards the specific continuum model assumptions of each analysis, as well as cross-calibration differences between *Suzaku* and *XMM-Newton*.

positive and negative first orders for each of the transmission gratings to obtain a single HEG and a single MEG data set. To preserve the higher spectral resolution of the HEG in the Fe *K* band, we did not co-add the HEG and MEG data for the following analysis.

2.2. Suzaku-XIS and HXD-PIN

MCG +8-11-11 was observed by *Suzaku* on 2007 September 17 for 100 ks (obsid 702112010), using the HXD nominal pointing. We followed a similar method of reducing the *Suzaku* data as described in detail by Bianchi et al. (2010), using the 2011 June 6 release of the *Suzaku* calibration files and `HEASOFT` version 6.11. For the observation with the XIS CCDs, we chose circular extraction regions with approximately 4.5 arcmin radii. For the XIS background we extracted spectra from source-free, rectangular regions (approximately 12 arcmin × 4 arcmin) near the edge of the chips. Individual spectra were extracted for each XIS CCD detector (i.e., XIS 0, XIS 1, and XIS 3) and separate data acquisition mode (3×3 and 5×5 mode), and then co-added during spectral analysis using the `ISIS combine_datasets` function. For the HXD we used only the PIN spectra, and adopted the cosmic X-ray background model recommended by the *Suzaku* ABC guide. The recommended cross-normalization of 1.18 was used between the PIN and XIS data throughout our analysis.

3. DATA ANALYSIS AND RESULTS

We analyzed the *Chandra* and *Suzaku* data using `ISIS` version 1.6.2. For both the HEG and MEG spectra, we grouped the data to a minimum signal to noise of 4.5 and two energy channels per bin, and considered data in the 0.7–7.5 keV and 0.5–7.0 keV range, respectively. For the *Suzaku*-XIS spectra we grouped the data to a minimum signal to noise of 6 and a minimum channel criterion that ensured that the binning was no finer than the half width half maximum resolution of the detector (see the description of this channel binning in Nowak et al. 2011). For the XIS spectra we considered data in the 0.8–1.7 keV and 2.4–9 keV range. For the HXD-PIN data we also binned to a minimum signal to noise of 6, and considered data in the 15–60 keV range. In all of our spectral fits, we used the Wilms et al. (2000) abundances and the photoelectric absorption cross sections of Verner et al. (1996). The assumed cosmological parameters are $H_0 = 73$ km s^{-1} Mpc^{-1}, $\Omega_\Lambda = 0.7$, and $\Omega_m = 0.3$. Unless otherwise noted, all spectral plots are in the rest frame of MCG +8-11-11. We quote statistical errors corresponding to 90% confidence for one interesting parameter ($\Delta\chi^2 = 2.71$).

3.1. Preliminary Analysis

To guide us in the adoption of an applicable global model, we first investigated the data with a phenomenological model, adding components as necessary to improve the fit. Here we outline the components required by the data.

3.1.1. Chandra-only fits

To begin, we focused on the HETG observation. The source is known to have significant neutral absorption in the line of sight, with a column density of the order of 10^{21} cm^{-2} (e.g., Dickey & Lockman 1990; Kalberla et al. 2005). Therefore, we first applied an absorbed power-law model, utilizing the `TBnew` absorption model (an improved version of the `TBabs` model of Wilms et al. 2000). This simple model provides a relatively good fit, yielding a reduced χ^2 value of 1.086 for 3119 degrees of freedom (DoF); however, see Section 3.1.2. A spectral index of $\Gamma = 1.743$ is found. There are clear residuals in the Fe *K* band near the rest energy of Fe Kα as expected, as well as in the MEG data below ∼1 keV. The flux-corrected[4] MEG and HEG spectra along with the model fit are shown in Figure 2.

Adding a Gaussian component to fit the residuals in the Fe *K* band gives a better fit (reduced $\chi^2 = 1.063$ for 3116 DoF, i.e., $\Delta\chi^2 = 75$) and a similar spectral index ($\Gamma = 1.75$). The rest-frame centroid of the Gaussian was found to be 6.40 keV, consistent with Fe Kα line emission, with a width $\sigma = 0.02$ keV.

Although there appears to be an absorption feature at ∼7.30 keV in the HEG data (in the rest frame, as seen in the bottom right panel of Figure 2), a significantly improved fit was not obtained when we attempted to model this feature and we conclude that it is a statistical fluctuation. We also note that there appears to be some soft excess below 1 keV, as seen in the MEG spectrum. We address this feature in Section 3.3.

3.1.2. Line-of-sight Absorption

We investigated the possibility of neutral absorption in the line of sight at the redshift of MCG +8-11-11 in addition to Galactic absorption. Considering only the MEG data in the 0.48–1 keV range and binning with a uniform 16 bins per channel, we applied two `TBnew` absorption models, one with no redshift and the other placed at the redshift of the source, to a power-law continuum and directly fitted (using Cash statistics; Cash 1979) the oxygen K-edge that is clearly detected in the MEG data. The `TBnew` model also describes the Fe L-edges and Ne K-edge present in the spectra. The 0.48–1 keV MEG data and model fit are shown in Figure 3. Although absorption local to the system is not required by the data, they are consistent with ∼1/3 (upper limit of ∼2/3) of the line-of-sight absorbing column being located at the redshift of MCG +8-11-11, with the remaining ∼2/3 (lower limit of ∼1/3) being Galactic absorption. Including two absorption components gives a slightly better fit: $C = 171$ with 169 data bins, compared to $C = 172.9$ with 169 bins for the fit with Galactic absorption alone. In this case, the total column density of the two components is consistent with the column density obtained from fitting with Galactic neutral absorption only (in both cases $N_{\rm H,\ los} \sim 0.24 \times 10^{22}$ cm^{-2}). In subsequent fits described here, for simplicity, we adopted a single neutral Galactic absorber.

3.1.3. The Warm Absorber?

Previous studies of MCG +8-11-11 described in Section 1 find evidence of warm absorption. With the exception of the Fe K region emission lines described below, we find no evidence of narrow line structure in either emission or absorption. To search for narrow line structure, we employed a Bayesian Blocks technique (based upon the algorithm of Scargle et al. 2013 that we have previously used in the study of HETG spectra of the low-luminosity AGNs, M81*; Young et al. 2007). Specifically, we fitted a phenomenological broadband continuum model to the MEG and HEG spectra (in this case an absorbed disk+powerlaw+Gaussian line), and compared the unbinned model counts and unbinned data counts to determine the optimal binning given a prior significance parameter, α, roughly equivalent to a significance threshold of $\exp(-\alpha)$.

[4] All flux-corrected spectra in this work have been created using solely the detector responses, and do not reference any assumed models.

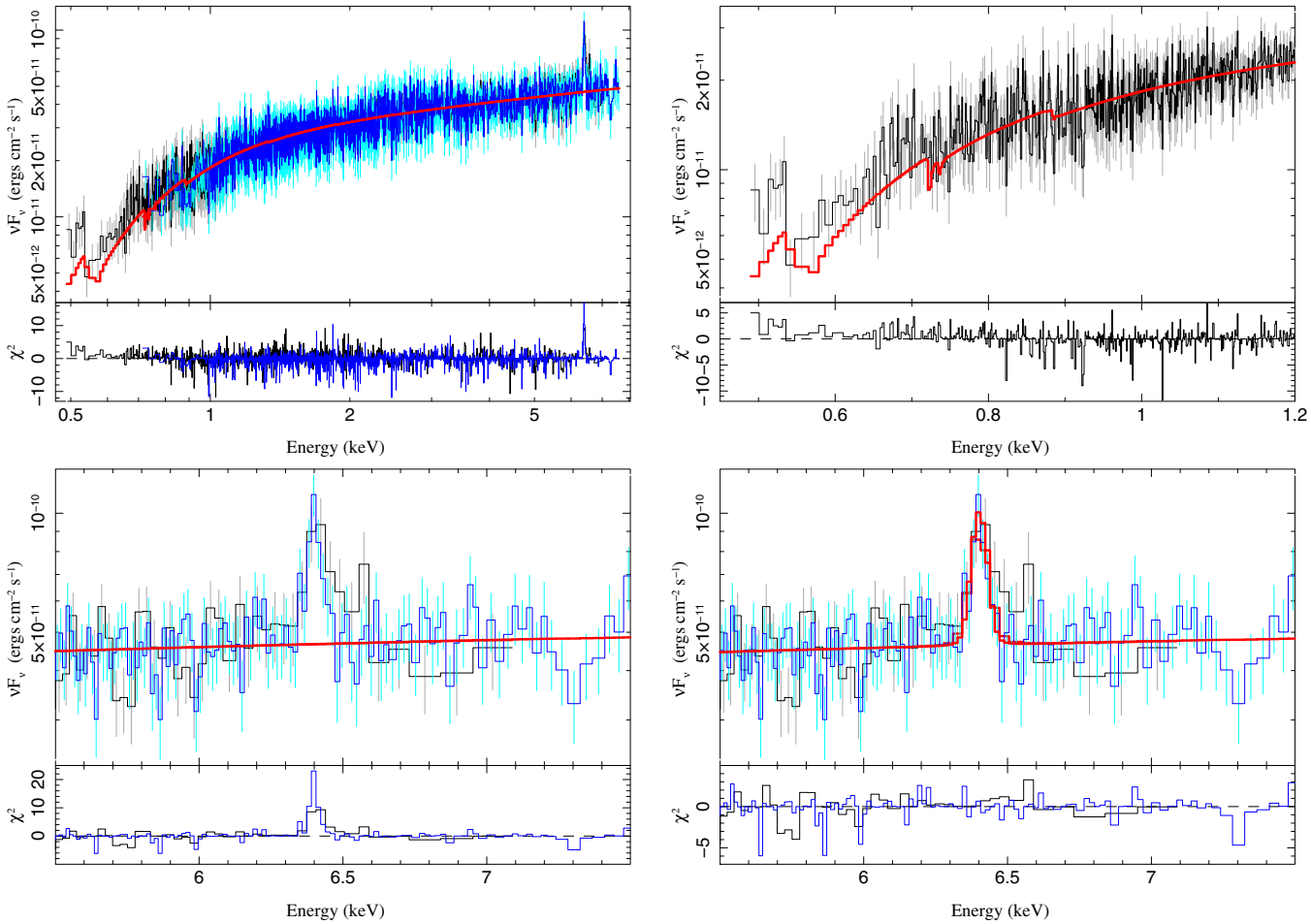

Figure 2. Top left and right and bottom left: a simple absorbed power-law model (red) was applied to *Chandra* MEG (black) and HEG (blue) spectra. Additionally, all spectra will be plotted in the source rest frame. The figure in the top left shows the full flux-corrected spectra. Close up views of the soft band (MEG only) and Fe *K* band are shown in the top right and bottom left panels, respectively; clear residuals are seen in the low-energy MEG spectrum and near the rest energy of Fe Kα. Bottom right: the model and flux-corrected spectra in theFe *K* band are shown after a Gaussian line is added to the model.

(A color version of this figure is available in the online journal.)

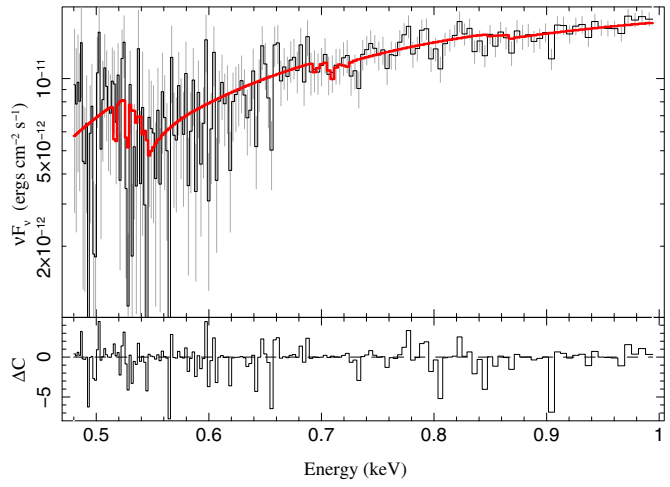

Figure 3. Direct fit of the O K-edge, Fe L-edges, and Ne K-edge, as observed by the HETG-MEG in its rest frame, using a simple power law and two line-of-sight absorption components, both modeled with `TBNew`. The data are consistent with an upper limit of 2/3 absorption local to MCG +8-11-11. The summed $N_{\rm H,\ los}$, including both extragalactic and Galactic contributions, is consistent with that found with Galactic-only absorption.

(A color version of this figure is available in the online journal.)

Significant emission or absorption lines would be indicated by narrow bins in the optimally partitioned spectrum for values of $\alpha \gtrsim 3$ (see the description of this procedure in Young et al. 2007). When applied to M81*, this method identified a significant number of emission lines, and a few absorption lines, at expected locations, with these line detections being verified by an independent Monte Carlo detection and fitting method. For the case of MCG +8-11-11, the Bayesian Blocks search did not reveal line features in either emission or absorption, in either the MEG or HEG spectra, at greater than 80% confidence levels ($\alpha \gtrsim 1.6$). This search included the region surrounding the "dip" at 7.30 keV, providing further evidence that the feature is not a real absorption line. We also performed a similar line search on the combined MEG and HEG data (unbinned to the MEG resolution, i.e., the HEG was binned by a factor of two), and again no line features were found at greater than the 80% confidence level. Our conclusion is that, in contrast to the prior suggestions, there is no evidence for a warm absorber in MCG +8-11-11.

Matt (2006) fit a number of absorption lines in the 0.5–1 keV range of their *XMM-Newton* spectra. Although none of these lines are indicated by the Bayesian Blocks analysis as being significant in the HETG spectra, we directly fitted these lines to determine upper limits to their equivalent widths. We binned

the MEG spectrum by a uniform factor of 16, and only considered absorbed power-law fits over the 0.48–1 keV range. Here we again apply Cash statistics as the number of counts per bin range only between 0–20 over the 0.48–0.7 keV band. The limits on the equivalent width depend upon the assumed width of the lines (a fitted line width is not given by Matt 2006), and here we fixed the line width to $\sigma = 1$ eV or $\sigma = 5$ eV. Fits included only a single absorption line at a time, with the energy fixed to the best-fit value reported by Matt (2006). We took a change of the Cash statistic of $\Delta C = 2.71$ as a proxy for the 90% confidence limit for a single interesting parameter.[5] With this criterion, the equivalent width (EW) limit is -2.9 eV/-1.2 eV ($\sigma = 5$ eV/1 eV) for the 526 eV line, -5.4 eV/-1.2 eV ($\sigma = 5$ eV/1 eV) for the 586 eV line, -4.1 eV/-1.3 eV for the 627 eV line ($\sigma = 5$ eV/1 eV), and -2.9 eV ($\sigma = 5$ eV) for the 654 eV line. All of the $\sigma = 1$ eV limits are of smaller magnitude than found with the fits of Matt (2006). Only for the case of $\sigma = 1$ eV for the 654 eV line was there any improvement in the fit statistic, where we found an EW of $-1.6^{+1.4}_{-1.0}$ eV. This is again of a smaller magnitude than for the fits by Matt (2006). We note, however, that this marginal detection is consistent with an unredshifted O VIII Kα line, as also noted by Matt (2006), and if real is unlikely to be associated with the AGNs. We further note that in the Bayesian Blocks analysis, although not formally significant, the 654 eV residual is actually the second most significant narrow residual, after an only slightly more significant narrow "absorption" feature coincident with the unredshifted forbidden line of Ne IX. This latter feature is not expected in a typical absorption model.

For the 999 eV line discussed by Matt (2006), we can also use the HEG data. Given the larger number of counts near this energy region, we applied a uniform binning of a factor of four to the MEG data, and a uniform binning of a factor of eight to the HEG data, and fitted an absorbed power law (again using Cash statistics) in the 0.8–1.1 keV band. The EW limit is -1.3 eV/-0.2 eV ($\sigma = 5$ eV/1 eV) for an absorption feature at this location. Again, this is of smaller magnitude than the absorption line fits of Matt (2006). We conclude that there is no compelling evidence for a warm absorber in the HETG spectra of MCG +8-11-11.

3.2. *Chandra* + *Suzaku* Fits

It was necessary to expand our data set to include the *Suzaku*-XIS and PIN spectra in order to further constrain the continuum and the emission in Fe *K* band.

The *Chandra*-HEG and MEG and the *Suzaku*-XIS and PIN spectra both reveal a typical absorbed power-law shape continuum and strong, narrow emission at the rest energy of Fe Kα. In Figure 4, we show a comparison of the HETG-HEG data to the XIS data, where we flux-corrected the combined HEG spectra and folded them through the *Suzaku* response, allowing for an overall "tilt" in spectral slope (centered at 3 keV) and cross-normalization constant. We found that although the *Chandra* and *Suzaku* data are not simultaneous, their similar shape facilitates global fitting. Specifically, the change in spectral slope was $\Delta\Gamma \approx 0.046$ with an HEG to XIS cross normalization constant of $\approx$0.96. These are within the likely cross-calibration differences of the two instruments (Ishida et al. 2011). (The residuals in the XIS spectra are predominantly known systematic effects in the *Suzaku* responses.) Given the similarity of these spectra, we proceeded to include all of the *Chandra*-HETG and *Suzaku*-XIS and PIN data in subsequent broadband fits, allowing a constant normalization factor between the fits to the data from the two missions. Note that the dip feature near 7.30 keV in the HEG spectrum is not seen in the XIS spectrum; however, we have not accounted for the statistical uncertainties in the HEG data in this comparison.

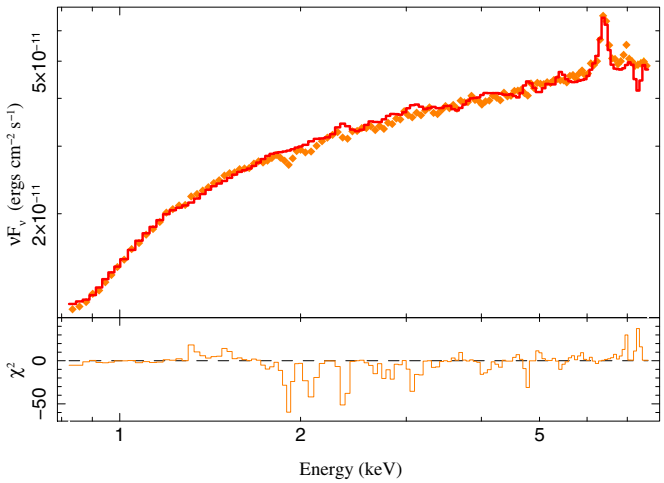

Figure 4. Comparison of *Chandra*-HETG (red) and *Suzaku*-XIS (black) spectra (see the text for details). Residuals are solely based upon the statistical errors of the *Suzaku*-XIS spectra and do not include the statistical errors of the HEG spectra.

(A color version of this figure is available in the online journal.)

We applied the phenomenological model consisting of a power-law spectrum, Galactic absorption, and Fe Kα line emission (as described above) to the four sets of spectra. This model yielded a worse fit than that found by fitting the *Chandra* data alone, giving a reduced χ^2 value of 1.140 for 3297 DoF.

Residuals consistent with Fe XXVI line emission are present in the XIS spectra (as expected from the results of previous studies; see Section 1) that are not evident in the HETG data. When we attempted to add a Gaussian line component to model Fe XXVI line emission in the HETG data alone, the centroid energy settled at 6.31 keV in the rest frame, with a line width $\sigma = 126$ eV. The added component may in fact have been attempting to model either a Compton shoulder for the Fe Kα emission line or underlying broadened Fe Kα line emission. We consider both of these possibilities in Section 3.3. Adding this Gaussian component to fit all four sets of data simultaneously (see Figure 5), on the other hand, resulted in a better fit (reduced $\chi^2 = 1.123$ for 3293 DoF, for a $\Delta\chi^2 = 61$), and the best-fit centroid energy of the Gaussian was consistent with Fe XXVI line emission. The top left panel of Figure 5 shows the flux-corrected MEG, HEG, XIS, and PIN spectra along with the model fit. A close up view of the Fe *K* band is shown on the right. For clarity we also show only the flux-corrected *Suzaku* spectra and model in the bottom panels. The *Suzaku*-XIS spectrum shows residuals redward of the Fe Kα line emission that could indicate a Compton shoulder and/or additional broad line emission. The *Chandra*-HETG spectrum shows additional soft excess in the continuum below $\sim$1 keV. Adding a thermal disk component (`diskbb`) to phenomenologically model the soft excess improves the fit (reduced $\chi^2 = 1.080$ for 3290 DoF, for a $\Delta\chi^2 = 145$), as seen in Figure 6. Although there are residuals in the XIS and MEG spectra that appear to be consistent with

[5] For the case of the 999 eV line discussed by Matt (2006) and below, where Gaussian statistics applied to the MEG data, there was no difference between the confidence limits if one uses a criterion of $\Delta C = 2.71$ or $\Delta\chi^2 = 2.71$. More properly, one could explore the Cash confidence limits with Monte Carlo simulations of the spectra. We have not performed such simulations.

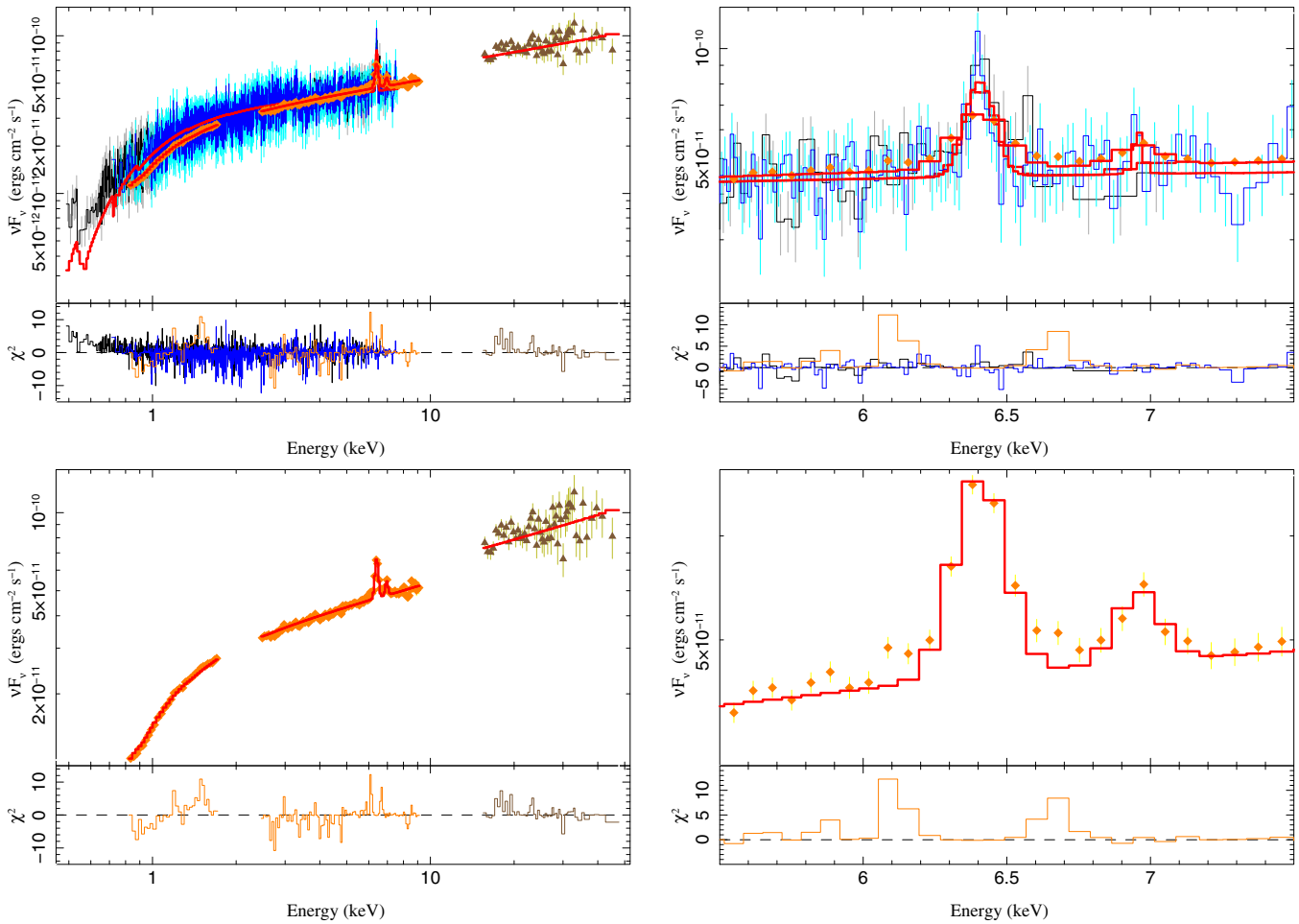

Figure 5. Flux-corrected spectra and fit for a phenomenological model including an absorbed power-law continuum and Fe Kα and Fe XXVI line emission. Top left: the flux-corrected MEG (black), HEG (blue), XIS (orange), and PIN (brown) spectra along with the model fit (red). Top right: a close up view of the Fe K region. Bottom left and right: as above, but showing only the *Suzaku* spectra to highlight the differences in the high-resolution gratings spectra and the CCD spectra. The right panels show residuals in the CCD spectrum that could indicated an Fe Kα Compton shoulder and/or additional broad line emission. The left panels show soft excess below $\sim$1 keV that is only probed by the MEG data.

(A color version of this figure is available in the online journal.)

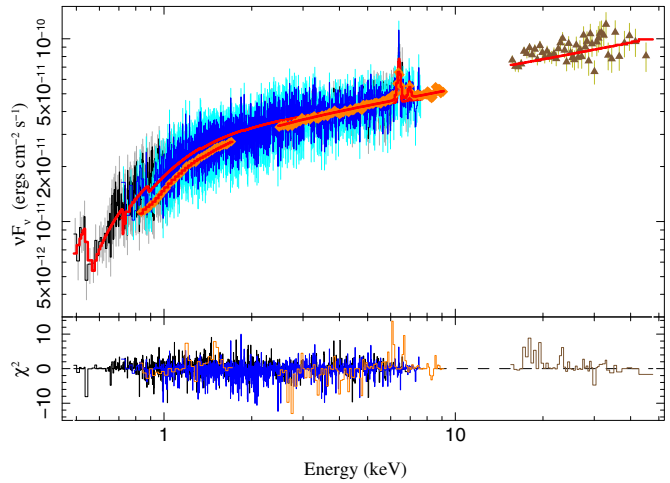

Figure 6. As described in Figure 5, with a soft excess component, phenomenologically described with `diskbb`, added to the model.

(A color version of this figure is available in the online journal.)

Fe XXV line emission, we did not find that an added Gaussian was required by the data.

As expected, utilizing both the *Chandra* and *Suzaku* data yields a more robust picture of the detailed emission and absorption mechanisms of the source since each of the instruments is suited to probe particular features in the spectrum. This preliminary investigation showed a combination of several possible spectral components, including an intrinsic power-law-shaped continuum, neutral line-of-sight absorption, soft excess, Fe XXVI line emission, and Compton reflection (including Fe Kα line emission with a possible Compton shoulder and/or broad Fe Kα line emission plus possible continuum curvature). We explore these features with more self-consistent models in the following section.

3.3. Modeling with Self-consistent Components

The combination of high spectral resolution *Chandra*-HETG data with broadband, high signal-to-noise *Suzaku* data allows us to constrain the physical parameters of the system by applying self-consistent X-ray spectral fitting models that have been recently developed. Physically based spectral fitting models offer a clear advantage over purely phenomenological ones as they allow us to extract more robust and physically meaningful constraints on each of the regions of an AGN, as well as the system as a whole. Our best-fit model consists of a power-law intrinsic continuum, soft excess (`diskbb`, included as a purely phenomenological component), Fe XXVI line emission, Galactic

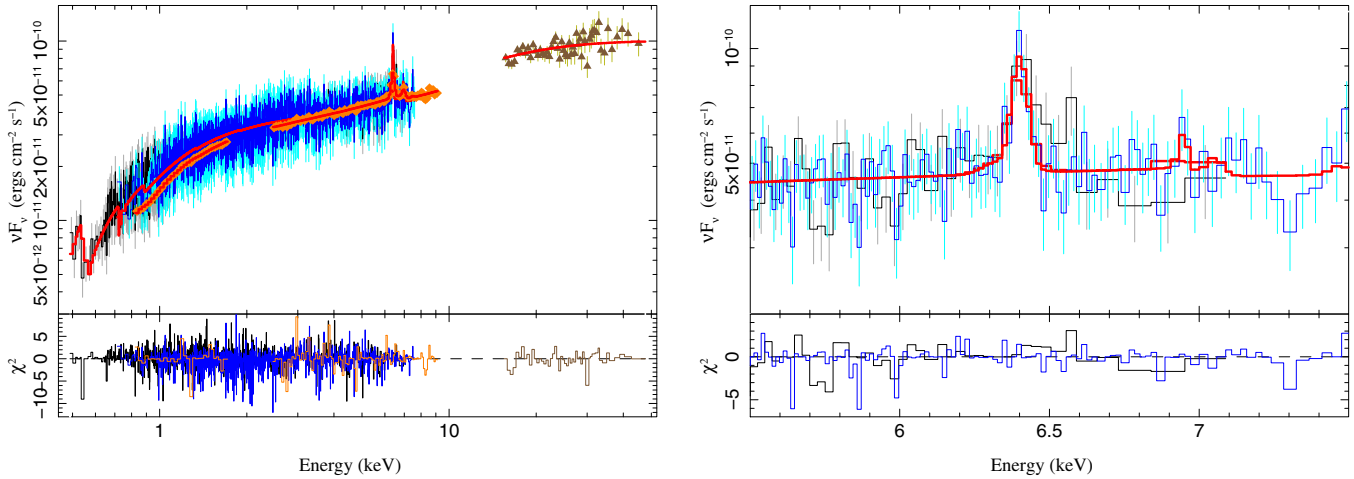

Figure 7. Flux-corrected spectra and fit for a model including an absorbed power-law continuum, soft excess, Fe XXVI line emission, and cold Compton reflection (PEXMON). Left: the flux-corrected MEG (black), HEG (blue), XIS (orange), and PIN (brown) spectra along with the model fit (red). Right: a close up view of the Fe K region for the HETG data only.

(A color version of this figure is available in the online journal.)

absorption (TBNew), and reprocessing by circumnuclear material. Below we describe the results of two sets of fits that utilize different models for the last component. In all of the fits, we allowed for some spectral variability between the *Chandra* and *Suzaku* observations. In particular, we did not tie the intrinsic power-law continua or the normalizations of the soft excess and the Fe XXVI line emission in the joint fits of those data sets.

Employing sophisticated models such as those discussed below is computationally expensive, especially when most of the model parameters are allowed to remain free. We therefore found it expedient to utilize a Monte Carlo Markov Chain (MCMC) code to fit the models to the data and to explore the parameter space as rigorously as possible. The code was developed specifically for ISIS, based upon the parallel "simple stretch" method from Foreman-Mackey et al. (2013) which in turn was based on the work of Goodman & Weare (2010).

For each MCMC run we created 200 (400) "walkers" which were evolved for 4700 (2500) steps for a total of 7.4×10^5 (3×10^6) samples for the MYTorus (PEXMON) model. Histograms and error bars are based on the last half of these samples (i.e., the first half were discarded as part of the MCMC "burn in").

3.3.1. Modeling with PEXMON

It is clear from our phenomenological fitting and from the literature (Matt 2006; Bianchi et al. 2010; Soldi et al. 2010) that MCG +8-11-11 likely includes a reflection component due to distant, cold, circumnuclear material. For comparison with previous results, in particular from Bianchi et al. (2010), and the results of fits with the MYTorus model (see Section 3.4.1), we modeled the reprocessor with PEXMON (Nandra et al. 2007). PEXMON is a self-consistent model that includes Compton reflection and fluorescent line emission (Fe Kα, Fe Kβ, and Ni Kα) from a slab of neutral material subtending a solid angle of 2π at the X-ray source (to represent reflection from an accretion disk, although it is sometimes used to describe reflection from a region such as the torus or BLR, as we do here for comparison with previous work).

The best-fit model spectrum is shown in Figure 7. The MCMC model parameters (reduced $\chi^2 = 1.048$ for 3288 DoF) and 90% confidence errors are given in Table 1. We obtained intrinsic power-law spectral indices of $\Gamma = 1.897^{+0.025}_{-0.025}$ (*Chandra*) and $\Gamma = 1.818^{+0.025}_{-0.015}$ (*Suzaku*). Although not tightly constrained, the 90% confidence range for the high-energy cutoff ($E_C = 155^{+223}_{-106}$) was consistent with the reported values measured by *Swift*-BAT, *BeppoSAX*, *OSSE*, and *INTEGRAL*. The neutral line-of-sight column density was slightly higher than that found in our preliminary analysis ($N_H \sim 0.39 \times 10^{22}$ as opposed to 0.24×10^{22} cm^{-2}); see Section 3.1.2. We modeled the soft excess, which was clear in the MEG residuals below $\sim$1 keV, with a simple disk component (Diskbb), finding a peak temperature of $kT = 0.091^{+0.007}_{-0.006}$ keV.

The Compton reflection fraction, $R = 3.04^{+0.42}_{-1.26}$, was higher than that reported by Bianchi et al. (2010) from their analysis of the *Suzaku*-XIS +PIN data. The inclination angle was found to be high, pegging the model limit of $\theta = 85$. The 68%, 90%, and 99% confidence contours of the reflection fraction versus photon index (left) and inclination angle (center) in Figure 8 shows the degeneracy of these parameters. In general, we see that lower inclination angles also allow for lower reflection fractions. It is important to point out, however, that the physical meaning of R, when this model is used in this capacity, is not clear. As discussed in MY09, there is no correlation between R and the column density of the distant reflector. R cannot simply be interpreted as a fraction of the subtended solid angle 2π, nor can it give a clear indication of reflection "strength" since that is geometry-dependent.

To 90% confidence, there is a large range in the abundance of Fe, with $A_{\rm Fe} = 0.65$–1.09. The PEXMON model was convolved with gsmooth to include the affects of kinematics. From this we found the width of the Fe Kα emission line at 6.4 keV to be $\sigma = 19^{+11}_{-13}$ eV, with a corresponding range in FWHM velocity of $\sim$950–7000 km s^{-1}, assuming Doppler broadening. This implies a distance of 0.014–0.76 pc to the Fe K line-emitting region from the black hole, assuming Keplerian motion and a black hole mass of $M_{\rm BH} = 1.2 \times 10^8\ M_\odot$ (Winter et al. 2010). In Figure 8 (right), we show confidence contours of the reflection fraction versus FWHM velocity width of the Fe Kα emission line.

For comparison, we considered only the *Chandra*-HEG data in the Fe K band using the same model. We further restricted the energy range to 5.8–7.2 keV, unbinned the data to achieve the maximum resolution of the HEG, and fit the model using

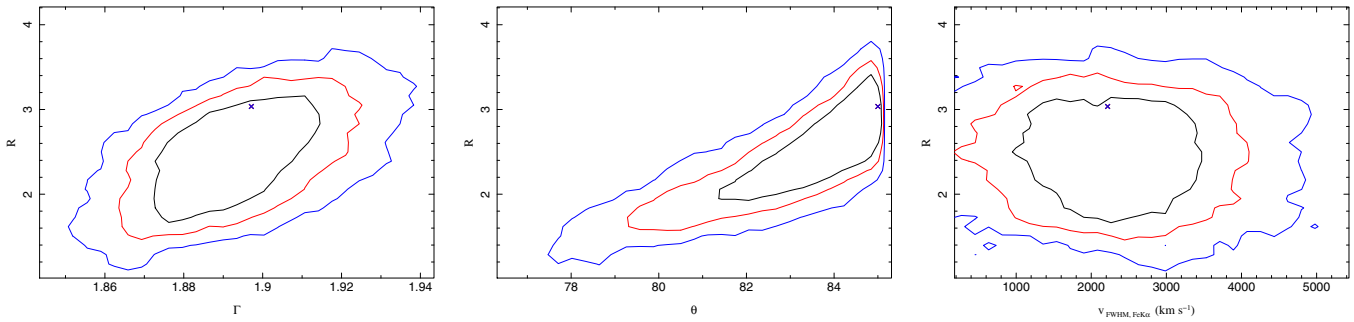

Figure 8. 68% (black), 90% (red), and 99% (blue) confidence contours for the model including PEXMON. Shown are contours for the reflection fraction vs. the spectral index of the HETG data (left), the inclination angle of the reflector (center), and the FWHM velocity width of the Fe Kα emission line.
(A color version of this figure is available in the online journal.)

Table 1
Global Fitting Results

Parameter	PEXMON Fit	MYTorus Fit
$N_{\rm H,\ los}$ (10^{22} cm^{-2})	$0.386^{+0.021}_{-0.018}$	$0.347^{+0.018}_{-0.005}$
$kT_{\rm disk}$ (keV)	$0.091^{+0.007}_{-0.006}$	$0.088^{+0.018}_{-0.007}$
$\Gamma_{\rm Chandra}$	$1.897^{+0.025}_{-0.025}$	$1.835^{+0.030}_{-0.012}$
$\Gamma_{\rm Suzaku}$	$1.818^{+0.025}_{-0.015}$	$1.744^{+0.015}_{-0.006}$
$N_{\rm PL,\ Chandra}$ (photons kev^{-1} cm^{-2} s^{-1} at 1 keV)	$0.0228^{+0.0045}_{-0.0014}$	$0.0196^{+0.0052}_{-0.0012}$
$N_{\rm PL,\ Suzaku}$ (photons kev^{-1} cm^{-2} s^{-1} at 1 keV)	$0.0177^{+0.0004}_{-0.0004}$	$0.0170^{+0.0004}_{-0.0001}$
$A_{\rm Fe}$	$0.86^{+0.23}_{-0.21}$	$1\,f$
R	$3.04^{+0.43}_{-1.27}$	...
$N_{\rm H,\ torus}$ (10^{24} cm^{-2})	...	$0.685^{+0.684}_{-0.128}$
θ (deg)	$85_{-5.6}$	$41.4^{+17.8}_{-30.4}$
$E_{\rm Fe_{K\alpha}}$ (keV)	$6.4\,f$	$6.404\,f$
$\sigma_{\rm Fe_{K\alpha}}$ (eV)[a]	20^{+42}_{-13}	25^{+37}_{-11}
$E_{\rm Fe_{K\beta}}$ (keV)	$7.05\,f$	$7.058\,f$
$E_{\rm Ni_{K\alpha}}$ (keV)	$7.47\,f$	$7.453^{+0.244}_{-0.239}$
$I_{\rm Ni_{K\alpha}}$ (10^{-6} photons cm^{-2} s^{-1})	...	$3.36^{+9.41}_{-3.04}$
$E_{\rm Fe\ XXVI}$ (keV)	$6.951^{+0.042}_{-0.018}$	$6.960^{+0.059}_{-0.054}$
$\sigma_{\rm Fe\ XXVI}$ (eV)	0^{+53}	0^{+97}
$I_{\rm Fe\ XXVI,\ Chandra}$ (10^{-6} photons cm^{-2} s^{-1})	$6.33^{+8.29}_{-6.33}$	$4.20^{+36.7}_{-3.58}$
$I_{\rm Fe\ XXVI,\ Suzaku}$ (10^{-6} photons cm^{-2} s^{-1})	$9.50^{+3.55}_{-3.56}$	$6.87^{+10.1}_{-3.70}$
χ^2 (DoF)	1.048 (3288)	1.058 (3288)
$F_{\rm 0.5-2\ keV}$ (10^{-11} erg cm^{-2} s^{-1})	2.51	...
$F_{\rm 2-10\ keV}$ (10^{-11} erg cm^{-2} s^{-1})	6.57	...
$F_{\rm 15-50\ keV}$ (10^{-10} erg cm^{-2} s^{-1})	1.08	...

Notes. Table 1 contains the results of the model fits described in Sections 3.3.1 and 3.4.1. 0.5–2 keV and 2–10 keV flux are for the HEG spectra, while the 15–50 keV flux is for the *Suzaku*-PIN spectrum. Errors are quoted at the 90% confidence level for one free parameter. Fixed parameters are denoted with "*f*".
[a] The Fe Kα and Fe Kβ line widths for both models, as well as the Ni Kα line width for the pexmon model, were obtained by convolving them with gsmooth, which gives a width at 6 keV. In the MYTorus fit, the Ni Kα emission line was constrained to have the same line width as Fe Kα. We therefore only quote the Fe Kα line width. The line intensities in these models are self-consistent with the other parameters of the models and are therefore not fit parameters. Line energies are in the rest frame of MCG +8-11-11.

Cash statistics. Figure 9 shows the HEG data and the model fit in this band. In this case, the Fe Kα emission line is resolved with a best-fit value of the Fe Kα emission line is $\sigma = 17^{+11}_{-9}$ eV, consistent with the global fit.

3.4. Relativistic Disk Emission?

Although the Fe K line emission and associated Compton hump appear to be well described by neutral reflection that is not relativistically smeared, there may be degeneracy between this and a relativistic and/or ionized component. We therefore included relativistically smeared, ionized reflection from an accretion disk (reflionx, Ross & Fabian 2005, convolved with relconv, Dauser et al. 2010) to investigate the contribution to the reflection continuum and Fe K line emission. Since broad Fe K line emission is better constrained by *Suzaku*, as a first step we considered those data alone. We tied the inclination angle

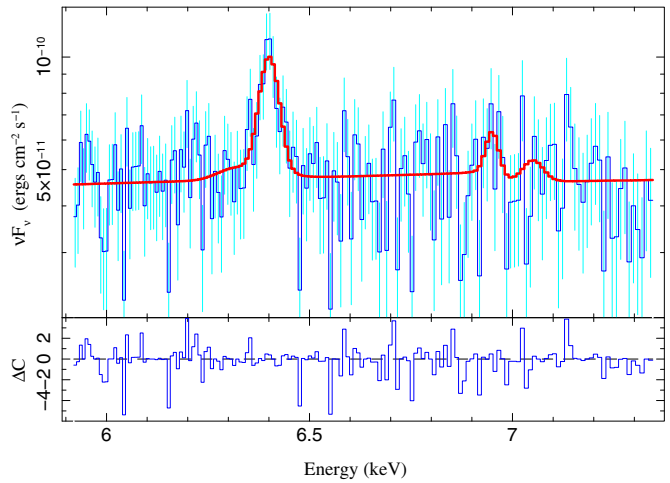

Figure 9. Flux-corrected HEG spectrum (blue) and fit (red) to the Fe *K* band for the model including PEXMON.

(A color version of this figure is available in the online journal.)

of the relconv smearing to that of the PEXMON component; however, we fixed the inner radius of the smearing to that of the marginally stable orbit for the fitted black hole spin (a^*) and the outer smearing radius to $400\,r_g$. We fixed the cutoff energy of the power law in the PEXMON model to be 300 keV (i.e., the value fixed in the reflionx model). We further tied the PEXMON and reflionx power-law indices and Fe abundances together, but left the reflionx ionization parameter to be freely fit.

We obtained a good fit to the data ($\chi^2 = 1.048$ for 169 DoF), with similar results to the *Chandra*-HETG +*Suzaku* fits without a relativistically smeared reflection component. The inclination was again found to be pegged at the PEXMON limit of 85°. We found a slightly harder power-law slope ($\Gamma = 1.78^{+0.05}_{-0.03}$) and a similar reflection fraction ($R \sim 2.0^{+0.8}_{-0.5}$) compared to the fit excluding relativistically smeared reflection from the accretion disk (see Table 1). The major differences for this model are that this fit implied an overabundance of Fe ($A_{\rm Fe} = 1.8^{+0.9}_{-0.8}$), and that some of the soft excess (≈1/3) is now ascribable to the soft end of the ionized reflection component (see Figure 10). This latter fact, however, is accompanied by an increase of the fitted $N_{\rm H}$ to $(5 \pm 1) \times 10^{21}$ cm^{-2}, which is slightly larger than indicated by direct fitting of the absorption edges in the HETG spectra.

With regard to the relativistic smearing parameters, the best fit spin was found to be at the maximal prograde limit of the relconv model, $a^* = 0.998$, with the lower limit being $a^* \geqslant 0.799$. The emissivity index for the relativistic smearing is $2.1^{+4.9}_{-0.3}$, i.e., consistent with being (but not required to be) dominated by emission from near the marginally stable orbit. For the lower range of the emissivity index, the width of the contributed Fe Kα line is, in fact, dominated by the ionization (with the fitted ionization parameter being $\Xi = 570^{+480}_{-240}$), rather than the relativistic smearing. The overall contribution of this reflection component is small, as seen in Figure 10. Over the ≈4–9 keV band it contributes ≈5%–8% of the flux, and allows for a small degree of extra curvature in the Fe line region. The overall normalization of the reflionx component is formally greater than zero at the 90% confidence level; however, we note that removing this component completely (i.e., removing four fit parameters: ionized reflection normalization and ionization parameter, black hole spin, and relativistic smearing emissivity index) only alters the best-fit absolute χ^2 by 8.5, with the fitted Fe abundance again becoming lower ($A_{\rm Fe} = 0.9 \pm 0.2$). As pointed out by Matt (2006), the existence of this component primarily serves to produce a reflection hump, without producing an associated narrow Fe Kα line component, thus allowing for higher Fe abundances in the unsmeared reflector.

Although the relativistically smeared, ionized reflection model does fill in some of the curvature around the Fe Kα emission line in the *Suzaku* data, its presence is not strongly required by the data. We therefore did not include relativistic disk emission in subsequent fits.

3.4.1. Modeling with MYTorus

We completed a similar analysis to that described in Section 3.3.1, using MYTorus (Murphy & Yaqoob 2009[6]; hereafter MY09) instead of PEXMON to model the cold reprocessor. MYTorus is a fully relativistic three-dimensional model that assumes a toroidal shape, but may also be used to model a cloud-like or "clumpy" geometry (see Yaqoob 2012 for details). The model does not presuppose a fixed distance from the nucleus nor does it assume the material is Compton-thick and therefore, for example, could be used to approximate absorption and

[6] See www.mytorus.com for more details.

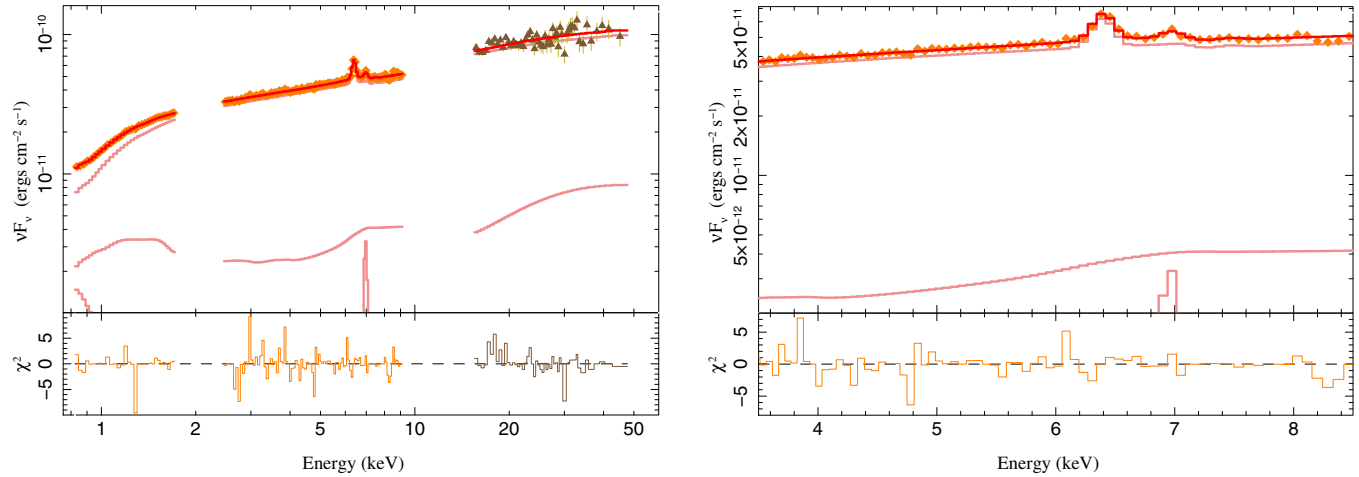

Figure 10. Left: *Suzaku* only fits with relativistically smeared ionized reflection. The individual PEXMON, soft excess, relativistically smeared reflection, and Fe XXVI components are shown. Right: close up of the Fe *K* band, also showing the individual model components.

(A color version of this figure is available in the online journal.)

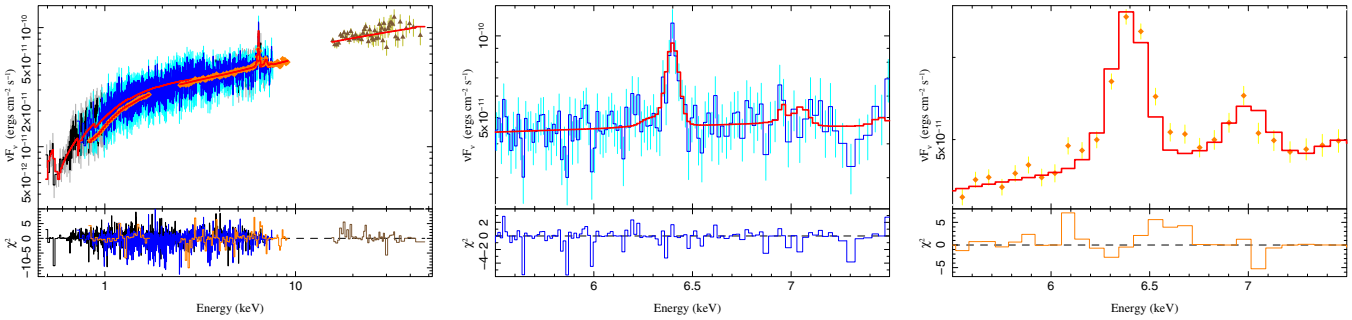

Figure 11. Flux-corrected spectra and fit for a model including an absorbed power-law continuum, soft excess, Fe XXVI line emission, and cold Compton reflection (MYTorus). Left: the flux-corrected MEG (black), HEG (blue), XIS (orange), and PIN (brown) spectra along with the model fit (red). Middle: a close-up of the Fe K region showing only the HEG data. Right: a close-up of the Fe K region showing only the XIS data.

(A color version of this figure is available in the online journal.)

reflection from the BLR. As MYTorus self-consistently models absorption, reflection, and Fe Kα and Fe Kβ line emission (including the associated Compton shoulders), it is more suitable for constraining the observed reflection component than purely phenomenological modeling. For this fit, we included Ni Kα line emission with a separate Gaussian component. Since the time-averaged signatures of the torus component are assumed to remain roughly constant, we do not allow for variability of this component between the *Chandra* and *Suzaku* observations. For the following, we set the relative normalization parameters of the scattered and line spectra to unity.

We assumed a terminal energy of 500 keV. The terminal energy of the MYTorus model is not the same as an observed cutoff in the power-law continuum but refers to the highest energy assumed for the intrinsic photons that were incident to the torus prior to absorption/reflection. The observed cutoff, which has previously been reported to be 101^{+48}_{-20} keV (*INTEGRAL* and *Swift* Soldi et al. 2010), 150^{+30}_{-20} keV (*Swift*; Bianchi et al. 2010), 170^{+300}_{-80} keV (*BeppoSAX*; Perola et al. 2000), and 270^{+90}_{-70} keV (*OSSE*; Grandi et al. 1998), can in fact be produced by Compton scattering of higher-energy photons in a Compton-thick medium (see MY09).

For comparison, we fitted the data utilizing a 200 keV terminal energy and found the same reduced χ^2 and consistent model parameters. Although we did not expect this difference in terminal energy to significantly affect the band that we fitted, it would potentially affect fits to higher-energy spectra (e.g., *Swift*). We defer an analysis including such data to later work. In the following, we report results from fits utilizing the 500 keV terminal energy MYTorus model tables.

Considering the degeneracies in the model parameters (e.g., between the photon index (Γ), the equatorial column density (N_H) of the torus, and the inclination angle (θ) of the torus), it is necessary to first coarsely and methodically explore the parameter space in order to avoid settling into a local minimum in χ^2. We thus determined that a face-on inclination angle (i.e., the torus is seen in reflection only) near $\theta \sim 40^\circ$ and an equatorial column density of approximately $N_H \sim 10^{24}\mathrm{cm}^{-2}$ is preferred by the model.[7]

In Figure 11, we show the model fit to the HEG, MEG, XIS, and PIN data, including a close up view of the Fe *K* band (middle and bottom panels). The best-fit parameters are given in Table 1. Leaving θ as a free parameter, we obtained a reduced χ^2 value of 1.058 for 3288 DoF. The derived values of the intrinsic power-law photon indices, $\Gamma = 1.835^{+0.030}_{-0.012}$ (*Chandra*) and $\Gamma = 1.743^{+0.006}_{-0.013}$ (*Suzaku*) are consistent with published values and those obtained in the PEXMON fit (Section 3.3.1). We obtained an inclination angle of $\theta = 41^{+18}_{-30}$ and an equatorial column density of $N_H = 0.69^{+0.68}_{-0.13} \times 10^{24}$ cm^{-2} for the torus, implying that the reflection in the spectrum is due to a possibly Compton-thick torus that is out of the line of sight.[8] Although the best-fit inclination angle is smaller than the inclination angle found in the PEXMON fit, we note that this is a model-dependent quantity in both cases. The toroidal column density and the reflection fraction obtained from the PEXMON fit are not physically similar parameters and should not be compared (see, e.g., MY09). In Figure 12 we show the 68%, 90%, and 99% confidence contours of equatorial column density versus photon index (left) and inclination angle (middle). As shown, N_H is well constrained even though the reprocessing material is out of the line of sight.

An energy offset for the MYTorus emission line model table was not required by the data, so the centroid energies of Fe Kα and Fe Kβ were intrinsically fixed by the model at 6.404 keV and 7.058 keV, respectively. Since the MYTorus model tables do not include kinematics, we convolved the emission lines with the Gaussian smoothing model gsmooth and constrained the Fe Kα, Fe Kβ, and Ni Kα line emissions to have the same velocity width. The width of the Fe Kα emission line was found to be $\sigma = 25^{+37}_{-11}$ eV, which corresponds to a range in FWHM velocity of 1648–7298 km s^{-1}. Assuming Keplerian velocity and a mass of $M_{\rm BH} = 1.2 \times 10^8 M_\odot$ (Winter et al. 2010), this places the reprocessing material at a distance of 0.013–0.25 pc from the central black hole. In Figure 11, we show the confidence contours of N_H versus FWHM velocity width, showing that, with this model, the width is constrained even to 99% confidence.

For the thermal emission from the disk, we obtained a peak temperature of $kT = 0.088^{+0.018}_{-0.007}$ keV, which was assumed to be constant during both the *Chandra* and *Suzaku* observations. The normalization of this component was higher for the *Chandra* data than the *Suzaku* data. Both of these results are similar to those obtained in fit described in Section 3.3.1.

4. CONCLUSIONS

We have analyzed the ~118 ks *Chandra*-HETG data together with ~100 ks of *Suzaku*-XIS +PIN data and found the following.

[7] For example, for fits where θ was fixed to 15°, 30°, 45°, 65°, and 85°, N_H was 1.42, 1.05, 1.16, 0.01, and 0.01 $\times 10^{24}$ cm^{-2} and the reduced χ^2 was 1.380, 1.057, 1.385, 1.259, and 11.389, respectively. Both edge-on cases were pegged at the lower limit of the model in N_H. In the face-on cases, Γ remained in the approximate range 1.75–1.85. For $\theta = 65^\circ$ and 85°, $\Gamma = 1.69$ (1.66) and 1.61 (1.44) for the *Chandra* (*Suzaku*) data and the fit to the Fe *K* band was (visibly) obviously inaccurate.

[8] By design, lines of sight through the torus would correspond to $60^\circ \leqslant \theta \leqslant 90^\circ$ (MY09).

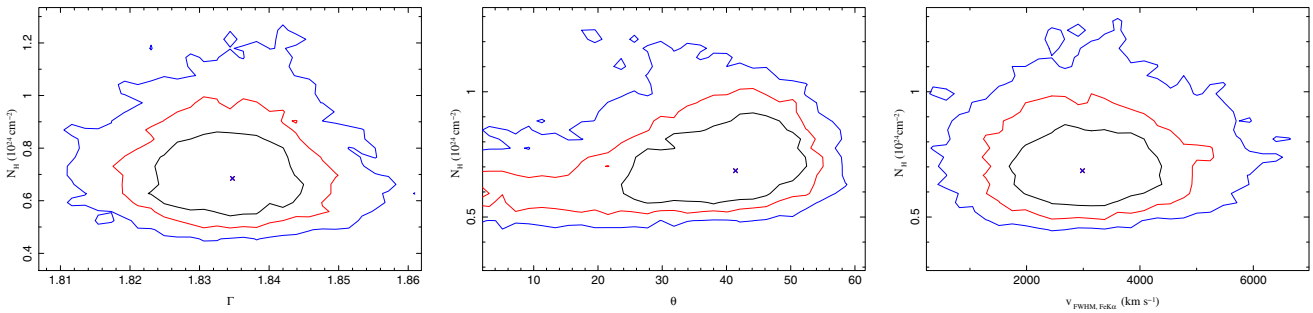

Figure 12. 68% (black), 90% (red), and 99% (blue) confidence contours for the model including `MYTorus`. Shown are contours for the equatorial column density of the torus vs. the spectral index of the HETG data (left), the inclination angle of the reflector (middle), and the FWHM velocity width of the Fe Kα emission line.
(A color version of this figure is available in the online journal.)

1. The Fe XXVI emission line previously reported in *Suzaku* studies of MCG +8-11-11 was marginally detected by *Chandra*.
2. Contrary to previous observations, the HETG data do not show significant evidence of warm absorption.
3. The MEG data reveal evidence of soft excess below the energy band probed by *Suzaku*. This soft excess is present whether the HETG spectra are fit alone or in conjunction with the *Suzaku* spectra.
4. The Compton reflection signatures are well described by material that is out of the line of sight. This is evident from the face-on inclination angle that is obtained using the `MYTorus` model for the reflector and since using the `PEXMON` model for this component did not require additional line-of-sight attenuation by cold, high column density material.
5. The reprocessor may be Compton-thick, and based upon the resolved width of the Fe Kα line is consistent with distances to the putative torus.
6. The narrow Fe Kα line emission and associated Compton shoulder fits both the *Chandra* and *Suzaku* data well. Although an underlying broad component fills in some of the residuals around the narrow line in the XIS spectrum, this component is not strongly constrained by the data. It primarily allows a higher Fe abundance to be fit for the unsmeared reflector component.

The *Chandra*-HETG data were crucial for investigating previous reports of a warm absorber and broad Fe Kα line emission in MCG +8-11-11. Our analysis leads us to conclude that neither of these components is required by the data. In terms of our `MYTorus` fits, the lack of a warm absorber is perhaps not surprising. In these models, the inclination angle is $\approx 40^{\circ}$, and possibly somewhat lower, indicating a more face on view of the system (assuming that the torus and inner disk regions are aligned). This could easily be outside of the opening angle of any warm absorbers. If we are looking more face on to the disk, however, why is reflection from a realtivistically smeared, ionized component not more prominent? The two most likely explanations for lack of such a feature would either be truncation of the inner disk regions (we consider the disk modeling of the soft excess to be a purely phenomenological description), or a reflection emissivity profile that is skewed away from the inner regions of the system. Without a convincing detection of a smeared, ionized reflection component, it is difficult to speculate further on its nature.

Although equally important to our investigation, *Suzaku*-XIS +PIN data alone were not capable of fully constraining any warm absorber component, nor the soft excess that was detected by *Chandra* below 1 keV. Careful modeling of both high spectral resolution and high signal-to-noise broadband data was required to show that the Fe K line emission is well accounted for with cold Compton reflection (the narrow line emission and associated Compton shoulder); additional sculpting of the Fe K region via warm absorption and/or relativistically broadened accretion disk reflection is unnecessary in this case.

Support for this work was provided by the National Aeronautics and Space Administration through *Chandra* Award Number GO1-12147X issued by the *Chandra* X-ray Observatory Center, which is operated by the Smithsonian Astrophysical Observatory for and on behalf of the National Aeronautics Space Administration under contract NAS8-03060.

REFERENCES

Bianchi, S., de Angelis, I., Matt, G., et al. 2010, A&A, 522, 64
Canizares, C. R., Davis, J. E., Dewey, D., et al. 2005, PASP, 117, 1144
Cash, W. 1979, ApJ, 228, 939
Dauser, T., Wilms, J., Reynolds, C. S., & Brenneman, L. W. 2010, MNRAS, 409, 1534
Dickey, J. M., & Lockman, F. J. 1990, ARA&A, 28, 215
Foreman-Mackey, D., Hogg, D. W., Lang, D., & Goodman, J. 2013, PASP, 125, 306
Garmire, G. P., Bautz, M. W., Ford, P. G., Nousek, J. A., & Ricker, G. R., Jr. 2003, Proc. SPIE, 4851, 28
Goodman, J., & Weare, J. 2010, Comm. App. Math Comp. Sci., 5, 65
Grandi, P., Haardt, F., Ghisellini, G., et al. 1998, ApJ, 498, 220
Houck, J. C., & Denicola, L. A. 2000, in ASP Conf. Ser. 216, Astronomical Data Analysis Software and Systems IX, ed. N. Manset, C. Veillet, & D. Crabtree (San Francisco, CA: ASP), 591
Ishida, M., Tsujimoto, M., Kohmura, T., et al. 2011, PASJ, 63, 657
Kalberla, P. M. W., Burton, W. B., Hartmann, D., et al. 2005, A&A, 440, 775
Matt, G. 2006, AN, 327, 949
Miller, L., Turner, T. J., & Reeves, J. N. 2009, MNRAS, 399, 69
Murphy, K. D., & Yaqoob, T. 2009, MNRAS, 397, 1549
Nandra, K., O'Neill, P. M., George, I. M., & Reeves, J. N. 2007, MNRAS, 382, 194
Nowak, M. A., Hanke, M., Trowbridge, S. N., et al. 2011, ApJ, 728, 13
Patrick, A. R., Reeves, J. N., Porquet, D., et al. 2012, MNRAS, 426, 2522
Perola, G. C., Matt, G., Fiore, F., et al. 2000, A&A, 358, 117
Reynolds, C. S., & Fabian, A. C. 1995, MNRAS, 273, 1167
Reynolds, C. S., & Nowak, M. A. 2003, PhR, 377, 389
Ross, R. R., & Fabian, A. C. 2005, MNRAS, 358, 211
Scargle, J. D., Norris, J. P., Jackson, B., & Chiang, J. 2013, ApJ, 764, 167
Soldi, S., Beckmann, V., Gehrels, N., et al. 2010, Eighth Integral Workshop. The Restless Gamma-ray Universe (INTEGRAL 2010), available online at http://pos.sissa.it/cgi-bin/reader/conf.cgi?confid=115
Verner, D. A., Ferland, G. J., Korista, K. T., & Yakovlev, D. G. 1996, ApJ, 465, 487
Wilms, J., Allen, A., & McCray, R. 2000, ApJ, 542, 914
Winter, L. M., Lewis, K. T., Koss, M., et al. 2010, ApJ, 710, 503
Yaqoob, T. 2012, MNRAS, 423, 3360
Young, A. J., Nowak, M. A., Markoff, S., Marshall, H. L., & Canizares, C. 2007, ApJ, 669, 830